Analysis of the Effect of Shrinkage on Macrosegregation in Alloy Solidification

MATTHEW JOHN M. KRANE and FRANK P. INCROPERA

Numerical calculations based on a continuum model are used to examine the effects of solidification shrinkage on the redistribution of solute in a Pb-19.2 pct Sn mixture which is convectively cooled at a sidewall. For each of three different cooling rates, separate calculations are performed for shrinkage- and buoyancy-induced flows, as well as for the combined influence of shrinkage and buoyancy effects. The calculations reveal that flow and macrosegregation patterns are more strongly influenced by buoyancy effects over a wide range of solidification rates. Although extremely large solidification rates yield small regions near the chilled wall in which shrinkage-induced flows control the redistribution of solute, the overall effect on macrosegregation is small relative to that associated with buoyancy. Scaling analysis of the governing equations produces reference shrinkage and buoyancy velocities which can be used to extend the current numerical results to other binary systems.

1. INTRODUCTION

RECENTLY, numerous studies have addressed means by which the solidification of binary metal alloys may be modeled, with particular attention given to continuum formulations based on classic mixing theory or volume averaging methods.[1–7] In these models, it is possible to track the freezing fronts without specifying interface conditions or explicitly computing the size of the different regions (solid, liquid, and mush). Important features of such models include prediction of the nonuniform redistribution of solute (macrosegregation) during freezing, as well as determination of growth rates for the solid and two-phase (mushy) regions and convection in the mush and bulk liquid. Recent successes include the prediction of channel development in the mushy zone for unidirectional solidification of an off-eutectic solution cooled from below and its relationship to the formation of freckle segregates in the final casting.[8,9] The freckles are regions of high concentration gradients in the frozen ingot and, therefore, of severe nonuniformity in mechanical properties.

Although the foregoing studies assume that the density of the alloy does not change during solidification, it is well known that most alloys shrink as they are cast. The attendant volume change can cause the casting to pull away from the mold wall and can induce defects such as hot tears and porosity. The objective of this study is to determine conditions under which shrinkage-induced flow significantly alters macrosegregation in a casting through its influence on concentration fields during freezing from a sidewall.

Many early attempts to model macrosegregation in binary alloys examined shrinkage effects as the only source of interdendritic liquid motion.[10,11,12] In these studies, all of which used globally stable Al-Cu mixtures chilled from below, experiments and analysis were in good agreement, showing the sometimes significant effect of solidification contraction on macrosegregation. Mehrabian *et al.*[13] extended the model to study side-cooled Al-Cu ingots in which buoyancy effects had a major role. They predicted that at higher solidification rates, shrinkage-induced flows would have a significant effect on the velocity field but that such effects would be negligible at lower rates. Lead-tin solutions were solidified from below at moderate freezing rates by Streat and Weinberg,[14] whose results indicated that for the solutally unstable cases (20 pct Sn), shrinkage does not play a significant role in macrosegregation.

The effect of shrinkage on the temperature field was considered by Chang and Tsai,[15] who numerically solved the governing equations for one-dimensional (1-D) freezing of a pure substance. An approximate solution to this problem is described by Viskanta.[16] Temperature and phase front histories predicted by Chang and Tsai indicate a negligible influence of solidification shrinkage.

Using a continuum model to simulate solidification induced at the sidewall of a mold, Xu and Li[17] were the first to examine the shrinkage phenomenon in a binary alloy (Cu-Al). They showed that a large pressure gradient is needed deep in the mushy zone to supply liquid to feed associated volume changes. Because the pressure gradient is orders of magnitude larger than that which could be generated by buoyancy forces, shrinkage-induced flows might be expected to dominate buoyant flows in regions close to the solidus. Xu and Li also showed macrosegregation patterns for the fully solidified ingot but did not compare them with predictions based on neglecting shrinkage effects.

Adapting the continuum model of Bennon and Incropera,[1] Chiang and Tsai[18,19] considered the effects of shrinkage on the solidification of a 1 pct Cr steel alloy. In their first article,[18] they computed velocity and temperature fields but neglected solutal redistribution. Shrinkage was accommodated by moving the free surface in a riser to account for the volume change at each time step. They obtained negligible differences between temperature histories predicted for conduction-dominated freezing and with inclusion of the effects of convection due to volume change, despite the use of a solidification contraction ratio, $\beta = (\rho_s/\rho_l - 1) = 0.2$, which substantially exceeds values normally associated with metallic systems ($0.02 \lesssim \beta \lesssim 0.10$).[20] In their second article, Chiang and Tsai[19] added the effect of natural convec-

MATTHEW JOHN M. KRANE, Research Assistant, and FRANK P. INCROPERA, Professor, are with the Heat Transfer Laboratory, School of Mechanical Engineering, Purdue University, West Lafayette, IN 47907.

Manuscript submitted August 19, 1994.

Table I. Material Properties and Casting Conditions

c_l = 177.9 J/kg K	T_e = 456 K
c_s = 154.7 J/kg K	T_0 = 560 K
D_l = 1.05 × 10^{-9} m²/s	T_c = 293 K
f_e^{Sn} = 0.619	β = 0.08
f_0^{Sn} = 0.192	β_s = 0.354
h_f = 30,162 J/kg	β_T = 1.09 × 10^{-4} K^{-1}
H = 0.05 m	κ_0 = 2.8 × 10^{-11} m²
k_l = 22.9 W/m K	μ_l = 0.0023 kg/s m
k_s = 39.7 W/m K	ρ_l = 10,000 kg/m³
L_1 = 0.2 m	ρ_s = 10,800 kg/m³
L_2 = 0.15 m	

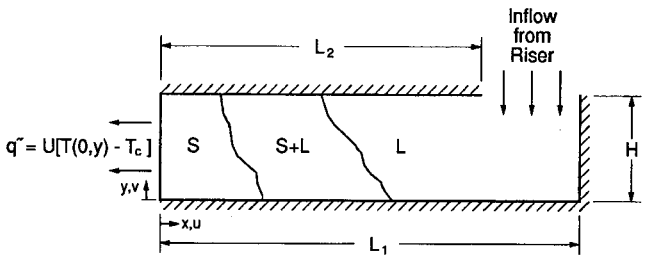

Fig. 1—System geometry.

tion due to temperature differences and performed three simulations: (1) with shrinkage-induced flow, (2) with buoyancy-induced flow, and (3) with both shrinkage- and buoyancy-induced flows. The authors concluded that (1) "although the isotherms and temperature fields (*sic*) in the casting caused by shrinkage and/or natural convection are usually the same, their flow patterns are different;" (2) volume change effects dominate flow patterns in the melt during the early and late stages of solidification, while thermally driven convection dominates in the interim; and (3) flows in the mushy zone are driven primarily by volume change rather than by natural convection. However, because they used a thermal expansion coefficient (β_T = 7.85579 × 10^{-9} K^{-1}), which is approximately five orders of magnitude smaller than the appropriate value of 1.26 × 10^{-4} K^{-1},[20] their conclusions should be viewed with caution.

In a similar study, Diao and Tsai[21] looked at a 4.1 pct wt Cu-Al system convectively cooled from below. They used the same version of the Bennon and Incropera model[1] adopted by Chiang and Tsai,[18] but this time they considered the effects of solute transport, and therefore macrosegregation, in the ingot. However, the geometry and choice of materials dictated thermally and solutally stable conditions. With no buoyancy-driven convection, it was the relative effects of diffusion and shrinkage-induced flow which were studied. The results showed that while there was a tendency for the rejected copper to diffuse upward and therefore to provide a more uniform distribution, the downward flow caused by volume change tended to overwhelm the effects of diffusion, causing more copper to be transported from the bulk liquid toward the solidus. Hence, solid close to the bottom of the ingot was predicted to be copper rich instead of slightly copper poor, as for diffusion-dominated conditions.

In the foregoing studies, no attempt was made to generalize the results. In fact, few attempts have been made to apply any sort of scale analysis to alloy solidification. Amberg[22,23] identified several dimensionless parameters for alloy freezing from a vertical boundary, deriving them from physically meaningful reference scales. These parameters were used to delineate different solidification regimes and to estimate the solidification time, global macrosegregation parameters, degree of undercooling, and onset of buoyancy-induced flows.

In this study, a numerical study is performed to identify the relative influence of shrinkage- and buoyancy-induced flows on macrosegregation. Also, the momentum equations are scaled inside the mushy zone to derive shrinkage and buoyancy reference velocities and to delineate the physical variables which govern shrinkage- and buoyancy-driven flows. The material used for these simulations is a Pb-19.2 wt pct Sn system, which has the advantages of a relatively simple phase diagram and well-known properties (Table I), as well as a large temperature range in the two-phase region and a large density difference between components. Both of these characteristics enhance macrosegregation. The alloy is chilled from a vertical side wall with an opening provided at the opposite side for a riser in the top surface (Figure 1). The size of the domain is L_1 = 200 mm, L_2 = 150 mm, and H = 50 mm.

II. MATHEMATICAL FORMULATION AND NUMERICAL METHODS

Simulation of the solidification of a binary metal alloy is considered in a two-dimensional domain. Adopting the continuum model of previous studies,[1,7] the equations of mass, momentum, energy, and species conservation are written in terms of the *mixture* density, velocity, enthalpy, and species concentration.

$$\frac{\partial \rho}{\partial t} + \frac{\partial}{\partial x}(\rho u) + \frac{\partial}{\partial y}(\rho v) = 0 \qquad [1]$$

$$\frac{\partial}{\partial t}(\rho u) + \nabla\cdot(\rho \mathbf{V} u) = \nabla\cdot\nabla\left(\mu_l \frac{\rho}{\rho_l} u\right) - \frac{\mu_l}{K_x}\frac{\rho}{\rho_l}(u - u_s) - \frac{\partial P}{\partial x} \qquad [2]$$

$$\frac{\partial}{\partial t}(\rho v) + \nabla\cdot(\rho \mathbf{V} v) = \nabla\cdot\nabla\left(\mu_l \frac{\rho}{\rho_l} v\right) - \frac{\mu_l}{K_y}\frac{\rho}{\rho_l}(v - v_s) + \rho_l g(\beta_T (T - T_0) + \beta_S (f_l^{\alpha} - {}^{\alpha}_{l,0})) - \frac{\partial P}{\partial y} \qquad [3]$$

$$\frac{\partial}{\partial t}(\rho h) + \nabla\cdot(\rho \mathbf{V} h) = \nabla\cdot\left(\frac{k}{c_s}\nabla h\right) + \nabla\cdot\left(\frac{k}{c_s}\nabla(h_s - h)\right) - \nabla\cdot(\rho(\mathbf{V} - \mathbf{V}_s)(h_l - h)) \qquad [4]$$

$$\frac{\partial}{\partial t}(\rho f^{\alpha}) + \nabla\cdot(\rho \mathbf{V} f^{\alpha}) = \nabla\cdot(\rho D_l \nabla f^{\alpha}) + \nabla\cdot(\rho D_l \nabla (f_l^{\alpha} - f^{\alpha})) - \nabla\cdot(\rho(\mathbf{V} - \mathbf{V}_s)(f_l^{\alpha} - f^{\alpha})) \qquad [5]$$

Although several terms in these equations are written as source terms, not all should be construed as such. This approach is motivated by the fact that many commonly available numerical codes employ the following standard form for advection-diffusion equations:

$$\frac{\partial}{\partial t}(\rho\phi) + \nabla\cdot(\rho V\phi) = \nabla\cdot\Gamma\nabla\phi + S \qquad [6]$$

In order to fit this form, where ϕ is a mixture quantity such as enthalpy, composition, or velocity, certain quantities must be artificially designated as source terms. For instance,

although the last two terms in Eqs. [4] and [5] are actually components of the advection and diffusion terms, they have been extracted to facilitate writing the conservation equations in the standard advection-diffusion form of Eq. [6]. Hence, as previously noted,[1] one must be careful when providing physical explanations for these "source-like" terms.

One such misunderstanding has arisen regarding the viscous diffusion terms in Eqs. [2] and [3]. For the x-momentum equation, this term can be divided into two parts:

$$\nabla\cdot\nabla\left(\mu_l\frac{\rho}{\rho_l}u\right) = \nabla\cdot(\mu_l\frac{\rho}{\rho_l}\nabla u) + \nabla\cdot\left(\mu_l u\,\nabla\left(\frac{\rho}{\rho_l}\right)\right) \quad [7]$$

or, assuming uniform densities for each phase,

$$\nabla\cdot\nabla(\mu_l\frac{\rho}{\rho_l}u) = \nabla\cdot(\mu_l\frac{\rho}{\rho_l}\nabla u) + \nabla\cdot(\mu_l u\left(\frac{\rho_s}{\rho_l}-1\right)\nabla g_s) \quad [8]$$

As noted by Prescott *et al.*,[7] when there is no density difference between the phases, viscous stresses arising from local density variations are negligible and the last term in Eqs. [7] and [8] is neglected. Although this term was included in the formulations of Tsai and co-workers, who examine the effects of volume change, it was misinterpreted. Chiang and Tsai[19] state that "shrinkage-induced flow is accounted for" by this term, and Diao and Tsai[21] note that this term "represent(s) the effect of shrinkage." However, in their derivation, Prescott *et al.*[7] have shown that the term represents a momentum sink resulting from viscous effects related to the different phase densities and is not a shrinkage source term.

Because the foregoing viscous term is not responsible for shrinkage-induced flow, the flow must be driven by some other mechanism. Tsai and co-workers[18,19,21] use a front tracking method, which relies on global mass continuity to determine the velocity perpendicular to a free surface in a riser. The average velocity of the free surface is then used to displace that surface, thus changing the domain size. In this study, the riser opening is modeled as a boundary of uniform velocity. This velocity is calculated at each time step and is determined by the mass inflow required to compensate for the volume change due to solidification during that time step. In both methods, shrinkage-induced flow arises from a need to satisfy Eq. 1 throughout the domain. However, the present method eliminates the need for changing the domain size. The effect of this velocity boundary condition is to trap tin-rich liquid in the ingot, rather than to let it escape to the riser, and, therefore, to produce more macrosegregation at that end of the ingot than would occur otherwise. The degree of overprediction depends on the size of the riser. If the riser is small, the tin-rich liquid would eventually be transported back into the mold by shrinkage, and the effect of the boundary condition on macrosegregation would be small. Such effects are ignored in this study and the results will show that this region is not one in which shrinkage-induced flows are important. Except for inflow at the riser, all other boundaries are impermeable and are governed by the no-slip condition.

Additional boundary conditions at the riser are prescribed by assuming inflow to have the initial composition of the melt and the riser itself to have the same local temperature as the melt at the boundary. Effectively, this is an insulated boundary condition ($\partial T/\partial y = 0$) at the opening of the riser. While these assumptions might cause some inaccuracies in the temperature and composition fields near the riser toward the end of solidification, they eliminate the need to calculate details of the riser and preserve the rectangular domain required by the numerical method.

The permeability components, K_x and K_y, in Eqs. [2] and [3] depend on the model linking the macroscopic equations to microscopic effects. Although many models have been proposed, we use the relatively simple Blake–Kozeny expression:[24]

$$K = \kappa_0\frac{g_l^3}{(1-g_l)^2}. \quad [9]$$

Because the anisotropy of the mushy region permeability is not well understood, it is assumed that $K_x = K_y = K$, with the permeability constant, κ_0, based on the dendritic arm spacing (DAS). A reasonable average value for the arm spacing in Pb-20 wt pct Sn (DAS = 71 μm) is provided by Nasser-Rafi *et al.*[25] and was used to compute the value of κ_0 cited in Table I.

The numerical scheme used to solve the conservation equations (the SIMPLER algorithm) is a control-volume-based finite difference method, with a fully implicit time marching technique.[26] The program uses a tri-diagonal matrix algorithm line-by-line solver with a block correction method, solving first for the pressure and velocity fields and then for the mixture enthalpy and composition. Using these mixture quantities, the linearized equilibrium phase diagram for Pb-Sn is then used with the lever law to determine the local temperature, the fraction solid, and the composition of the solid and liquid phases. Use of the lever law, rather than the Scheil model, results in less eutectic solid in the final casting. (The model can account for both primary and eutectic solidification). However, experimental work by Wang *et al.*[27] and numerical work by Schneider and Beckermann[28] indicate that the actual production of eutectic solid may be much lower than that predicted by the Scheil model, except near the regions which are last to solidify. The expressions based on the phase diagram are well documented[1,24] and are not repeated here. The grid (85 × 41) provides a compromise between computational accuracy and speed and is comparable to that used in a previous simulation of a lead-tin system.[29] The system was initially at a uniform temperature (T_0 = 560 K) before being cooled at the left wall. The thermal boundary condition is prescribed as

$$q'' = U[T(0,y) - T_c] \quad [10]$$

where the overall heat-transfer coefficient, U, can account for heat transfer by combined modes from the inner surface of the mold wall at $T(0, y)$ to a heat sink at a fixed chill temperature, T_c. Three different values of the overall heat-transfer coefficient were used (U = 10^2, 10^3, and 10^4 W/m^{2}K), ranging from very slow solidification to rapid solidification associated with a boundary condition which is *nearly* isothermal. All other solid walls are adiabatic, and with the exception of the riser, all boundaries are impermeable to species transport. The largest time steps which yielded quickly converged results varied with cooling rate,

ranging from 0.5 to 0.05 seconds for slow and rapid cooling, respectively. Solutions were considered converged if they had residuals of mass, energy, and species less than 10^{-4} for at least five consecutive iterations. The calculations were performed on an HP-715* workstation and used approximately 250 CPU seconds per time step.

*HP-715 is a trademark of Hewlett-Packard Company, Colorado Springs, CO.

III. SCALE ANALYSIS

To enhance interpretation of the numerical results of this study, a scaling analysis is performed for equations pertinent to the mushy zone within which flow strongly influences redistribution of the components during freezing. The method used to determine a reference velocity in the mushy zone for buoyancy-induced flow follows the approach adopted by Bejan.[30] Equations [2] and [3] are derived assuming that deep inside a mushy zone, characterized by a rigid solid, D'Arcy forces dominate the resistance to flow and transient, advective, and diffusive effects can be neglected.[7] Therefore, Eqs. [1] through [3] can be approximated as

$$\frac{\partial(\rho u)}{\partial x} + \frac{\partial(\rho v)}{\partial y} \sim 0 \qquad [11]$$

$$-\frac{\mu_l}{K}\frac{\rho}{\rho_l} u \sim \frac{\partial P}{\partial x} \qquad [12]$$

$$-\frac{\mu_l}{K}\frac{\rho}{\rho_l} v \sim \frac{\partial P}{\partial y} + \rho g[\beta_T(T - T_0) + \beta_S(f_l^\alpha - f_{l,0}^\alpha)] \qquad [13]$$

Differentiating Eqs. [12] and [13] with respect to y and x, respectively, and subtracting one from the other to eliminate the pressure gradients, it follows that

$$\frac{\mu_l}{K}\frac{1}{\rho_l}\left(\frac{\partial \rho u}{\partial y} - \frac{\partial \rho v}{\partial x}\right) \sim \rho_l g\left(\beta_S \frac{\partial f_l^\alpha}{\partial x} + \beta_T \frac{\partial T}{\partial x}\right) \qquad [14]$$

However, because $(\beta_s \Delta f_l^\alpha / \beta_T \Delta T) >> 1$ for Pb-Sn, as well as for many other liquid metal alloys, only the solutal buoyancy force will be retained in subsequent considerations, although similar results are readily obtained for the thermal buoyancy force. With freezing from the side, the mushy zone thickness, δ, and the height of the domain, H, are used as length scales ($x \sim \delta$, $y \sim H$), and the three remaining terms of Eq. [14] may be scaled as u/H, v/δ, and $(\rho_l g \beta_s \Delta f_l^\alpha K)/(\mu_l \delta)$. The liquid composition difference is the difference between the initial value and the composition of the liquid as the mixture approaches the solidus line, $\Delta f_l^\alpha = (f_0^\alpha - f_{l,s}^\alpha)$.

From continuity, it follows that $u/\delta \sim v/H$, or $(u/H)/(v/\delta) \sim (\delta/H)^2$. If the ingot has an aspect ratio of order unity, δ/H may range from much less than unity to order unity during the course of solidification. Thus, u/H is initially much less than v/δ and becomes, at most, of order v/δ as solidification proceeds. From Eq. [14], we obtain

$$v/\delta \sim \frac{\rho_l g \beta_S \Delta f_l^\alpha K}{\mu_l \delta} \qquad [15]$$

which provides an order-of-magnitude estimate of the buoyancy driven flow velocity in the mushy zone. That is, with $U_b \sim v$,

$$U_b \sim \frac{\rho_l g \beta_S \Delta f_l^\alpha K}{\mu_l} \qquad [16]$$

Because the permeability, K, varies widely over time and space, Eq. [16] should be interpreted as a *local* estimate of the strength of the buoyancy-induced flow.

To obtain an order-of-magnitude estimate of the shrinkage-induced velocity, U_s, the two-phase region is treated as a control volume for which mass inflow is balanced by mass storage. That is,

$$\rho_l A_m U_s = \frac{dm}{dt} = (\rho_s - \rho_l)\frac{dV_s}{dt} \qquad [17]$$

where A_m is the frontal area of the mushy zone. This area may be approximated as the product of the mold height and a unit depth ($A_m \approx H \cdot 1$). It follows that

$$U_s \sim \left(\frac{\rho_s - \rho_l}{\rho_l}\right)\frac{1}{H}\left(\frac{1}{\rho_s}\frac{dm}{dt}\right) \qquad [18]$$

If the solidification rate is expressed as

$$\frac{dm}{dt} = q_{\text{lat}} / h_f \qquad [19]$$

where q_{lat} is the rate at which latent heat is removed from the mushy zone, the shrinkage-induced velocity may be approximated as

$$U_s \sim \frac{\beta q_{\text{lat}}}{H \rho_s h_f} \qquad [20]$$

The heat released due to freezing, q_{lat}, is of the same order as that removed through the mold wall, particularly during the early stages of solidification.

IV. NUMERICAL RESULTS AND DISCUSSION

To assess the influence of solidification shrinkage, nine numerical simulations were performed. The objective was to determine if and when shrinkage-induced flows are vigorous enough to significantly affect the redistribution of solute. For each value of U, three numerical simulations were performed, corresponding to (1) buoyancy-induced flow ($\rho_s = \rho_l$), (2) combined buoyancy- and shrinkage-induced flow, and (3) shrinkage-induced flow ($\beta_s \approx \beta_T \approx 0$). In each case, the simulations were taken to the point of complete solidification. Numerical results are restricted to the consideration of component redistribution and macrosegregation effects. They are presented as plots of tin concentration over the entire domain at various times and, to facilitate comparisons for the three flow conditions, as plots of the tin concentration along the midheight of the ingot.

The thermal boundary condition for the slowest freezing rate case ($U = 100$ W/m^2 K) is close to that considered in previous laboratory experiments and numerical studies.[21,29,31] The overall coefficient can be achieved by transferring heat by radiation and conduction over a small air gap between the mold and a cold plate maintained near room temperature. With this boundary condition, the ingot was completely solidified in just under 6000 seconds.

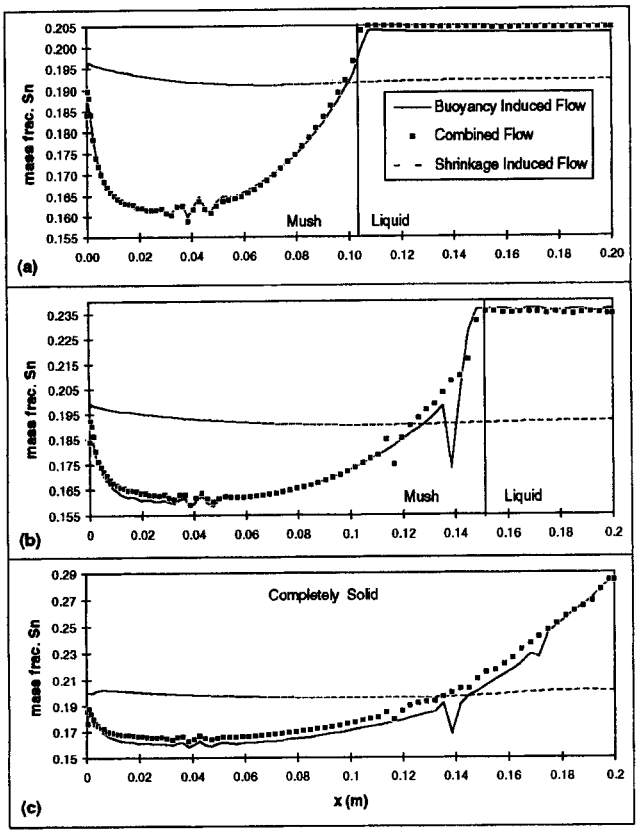

Fig. 2—Midheight composition profiles, U = 100 W/m² K, at (*a*) 1000 s, (*b*) 2000 s, and (*c*) 6000 s.

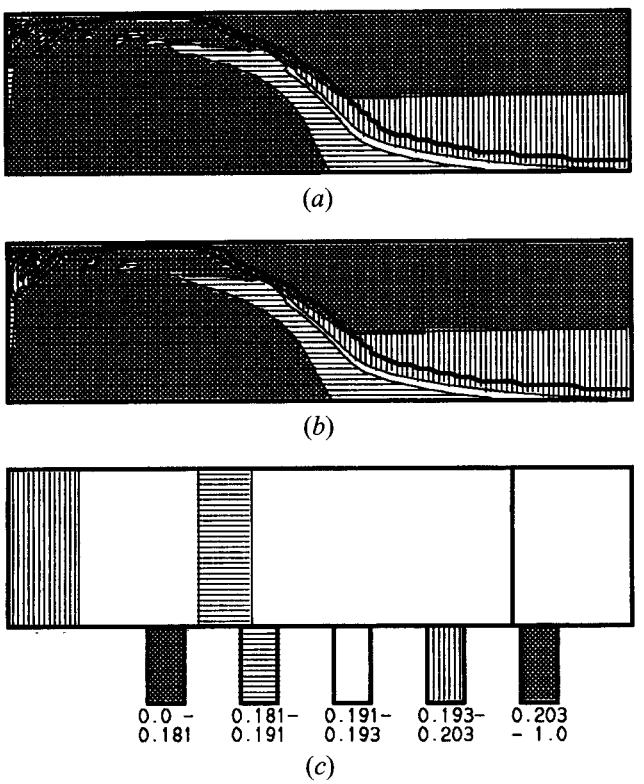

Fig. 3—Macrosegregation plots at 1000 s for U = 100 W/m² K: (*a*) buoyancy-induced flow, (*b*) buoyancy- and shrinkage-induced flow, and (*c*) shrinkage-induced flow.

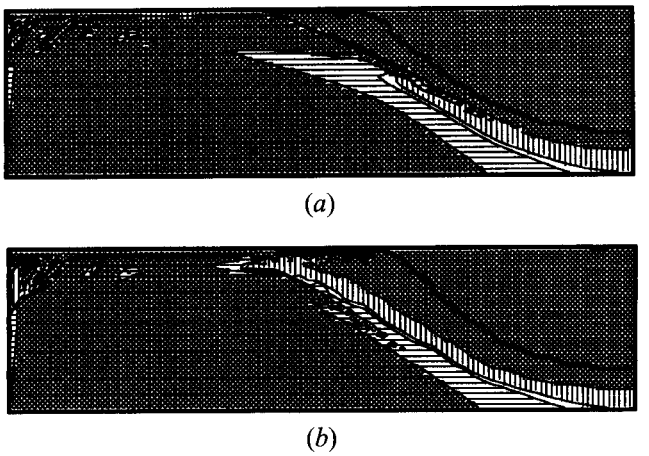

Fig. 4—Macrosegregation plots at 2000 s for U = 100 W/m² K: (*a*) buoyancy-induced flow and (*b*) buoyancy- and shrinkage-induced flow (same legend as in Fig. 3).

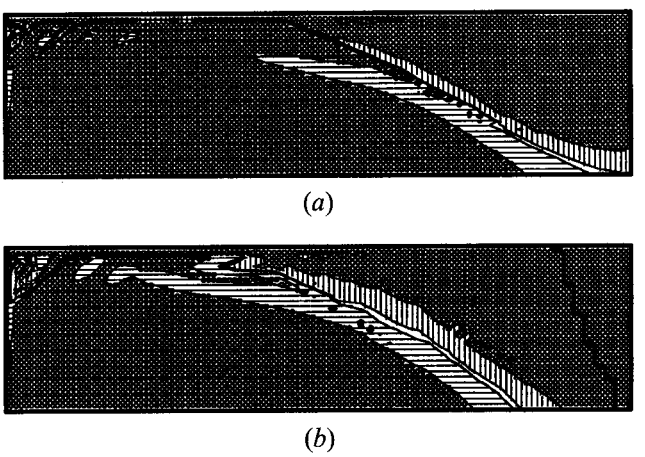

Fig. 5—Macrosegregation plots at 6000 s for U = 100 W/m² K: (*a*) buoyancy-induced flow and (*b*) buoyancy- and shrinkage-induced flow (same legend as in Fig. 3).

The redistribution of solute for this first case is shown in Figure 2, which provides the midheight composition at 1000, 2000, and 6000 seconds for the three flow conditions, and in Figures 3 through 5, which indicate the extent of macrosegregation for the entire domain at the selected times. From the excellent agreement between predictions for the buoyancy and buoyancy/shrinkage–driven flows, it is evident that throughout the solidification process, shrinkage has only a small, if not negligible, effect on macrosegregation. The combined flow results reveal that very close to the chilled wall, there is a small band of negative segregation. This negative segregation was also predicted by Schneider and Beckermann,[28] who, after a careful numerical study using U = 75 W/m² K, concluded that this segregation is due to the diffusion of solute in the liquid at the very early stages of solidification. However, it does not occur at the higher heat extraction rates of the present work. In those cases, described subsequently, the shrinkage-induced velocities are significantly higher at early times and the advection of solute toward the chill surface overwhelms the effect of diffusion away from the surface.

The distribution of solute at t = 1000 seconds is shown in Figures 2(a) and 3. When the flow is driven only by solidification contraction, there is a small increase in tin

concentration near the chilled wall and a correspondingly slight reduction further in the mushy zone. The small magnitude of the segregation is similar to that found by Schneider and Beckermann[28] using a different model. This condition results from the 1-D velocity field, which is perpendicular to the gravity vector and draws tin-rich interdendritic fluid toward the cold wall.[21] Macrosegregation patterns for the two cases with buoyancy-driven flows are very different from that associated solely with shrinkage but are very similar to each other. When present, buoyancy effects are strong enough to move the rejected tin upward and out of the mush, into the bulk liquid along the top wall. In the combined case, shrinkage does have a small effect on macrosegregation in the upper left corner of the domain. There is some evidence of channels forming in that region, induced by solutal remelting of the dendritic structure. Because some tin-rich liquid is drawn toward the chilled wall, remelting and consequent channeling are predicted closer to the wall for the combined case than for buoyancy alone. Near the top of the mushy zone, the flows are slowed and turned by the top wall, allowing shrinkage to have a small effect, while at the midheight, the buoyancy-driven flow overwhelms the shrinkage driven flow, as seen in Figure 2(a). As the mushy zone slowly develops and buoyancy-driven flow expels tin-rich liquid into the melt, a large zone of negative segregation is produced inside the mush. In that zone, the midheight profiles show some irregularities, which are small channels forming due to local solutal remelting.

With increasing time, the two-phase region continues to widen. At $t = 2000$ seconds (Figures 2(b) and 4), the liquidus front is at $x \approx 150$ mm at the midheight, while at the chilled wall, the solid fraction is still less than unity, $g_s(x = 0) \approx 0.9$. The mush is now large enough to include the tin-rich section created by the earlier expulsion of liquid from the mushy zone. Close inspection of the macrosegregation patterns in Figures 4(a) and (b) shows again that several tin-rich areas are slightly closer to the cold wall for the combined flow, but there is still little qualitative difference between the two. As seen in Figure 2(b), the influence of shrinkage remains the same, involving a small rise in Sn near the chilled wall and a slight decrease inside the mush near the liquidus front. Because conditions are nearly 1-D, the full macrosegregation patterns caused by shrinkage-driven flows will only be shown when necessary.

In the completely solidified ingot at $t = 6000$ seconds (Figures 2(c) and 5), the final macrosegregation plots show some influence of shrinkage in the combined case, where tin-rich regions are slightly shifted toward the cold wall compared to the buoyancy case. In the final stages of solidification, the shrinkage becomes relatively more important, as the permeability and the composition gradients decrease. The shrinkage midheight profile (Figure 2(c)) is qualitatively the same as the profiles at the previous times and indicates relatively mild macrosegregation compared to the large spatial variations in composition caused by buoyancy-induced flows.

The low heat-transfer coefficient of the foregoing case results in a relatively low latent heat release rate and, therefore, a weak shrinkage effect. The second case corresponds to an order of magnitude increase in the heat-transfer coefficient ($U = 1000$ W/m^2 K) and hence to much higher values of q_{lat}, especially during the early stages of solidification when the difference between the wall (T_w) and sink (T_∞) temperatures is large. The wall temperature decays more rapidly than in the first case but not fast enough to be approximated as an isothermal boundary.

Figure 6 shows midheight composition profiles at times ranging from 25 to 1750 seconds (complete solidification). In Figure 6(a) ($t = 25$ seconds), profiles for the shrinkage and combined flows match almost exactly, with discernable differences existing only in proximity to the liquidus front. As indicated by Eq. [16], the buoyancy velocity increases with the permeability, and if deviations from a shrinkage dominated flow occur, they do so first at the liquidus ($K \Rightarrow \infty$). At 50 seconds (Figure 6(b)), a completely solid region begins to form at the chilled wall, and near this interface, solutal redistribution is still dominated by the shrinkage-induced flow. However, as the liquidus front is approached, the tin concentration begins to follow the predictions based on a buoyancy-induced flow. Note that the concentration at the far end of the mold ($x = 200$ mm) increases slightly, as tin-rich liquid escapes the mushy zone and begins to displace the bulk liquid.

Macrosegregation over the entire domain at 50 seconds is shown in Figure 7 for all three flow conditions. While the Sn concentration in the near wall region remains close to the initial composition for the buoyancy-induced flow (Figure 7(a)), the shrinkage flow (Figure 7(c)) yields elevated tin concentrations in this region. This result suggests that while the shrinkage-induced flow transports tin-rich liquid toward the chilled surface, buoyancy forces are insufficient to transport interdendritic liquid very far before it is overtaken by the freezing front. As solidification progresses, buoyancy-induced flow does begin to advect a significant amount of tin-rich liquid up and out of the mush, creating the conelike segregates of Figures 7(a) and (b). A comparison of the two cones shows that shrinkage affects the cone shape, making it look more like the tin-depleted band in Figure 7(c). At the midheight (Figure 6(b)), the combined flow yields a much lower Sn concentration in the middle of the mush, where buoyancy *and* shrinkage are both important, with buoyancy causing the tin to ascend, while shrinkage pulls it toward the chilled wall. The first effect causes tin-depleted liquid to ascend from lower regions of the mush to the central region, while the second effect causes fluid at the initial composition to be drawn in from the melt.

Figures 6(c) through (e) show a progression of midheight concentration profiles during a transitional time in which shrinkage loses its ability to significantly affect the fluid flow. As the wall temperature decreases, thereby decreasing q_{lat}, the shrinkage-induced velocity (U_s) decreases proportionally. At $t = 100$ seconds, the profiles are similar to those at 50 seconds but with significantly more macrosegregation for the combined predictions. This increase in macrosegregation is entirely due to the increased influence of buoyancy-driven solute redistribution. For $t = 200$ seconds, shrinkage effects cease to dominate at any location in the mushy zone, and for $t = 400$ seconds, shrinkage-induced flow ceases to have any discernable effect within the mushy zone. Macrosegregation plots for the entire domain at 200 seconds (Figure 8) reveal a vestigial influence of shrinkage, with Figure 8(b) exhibiting a larger cone than Figure 8(a).

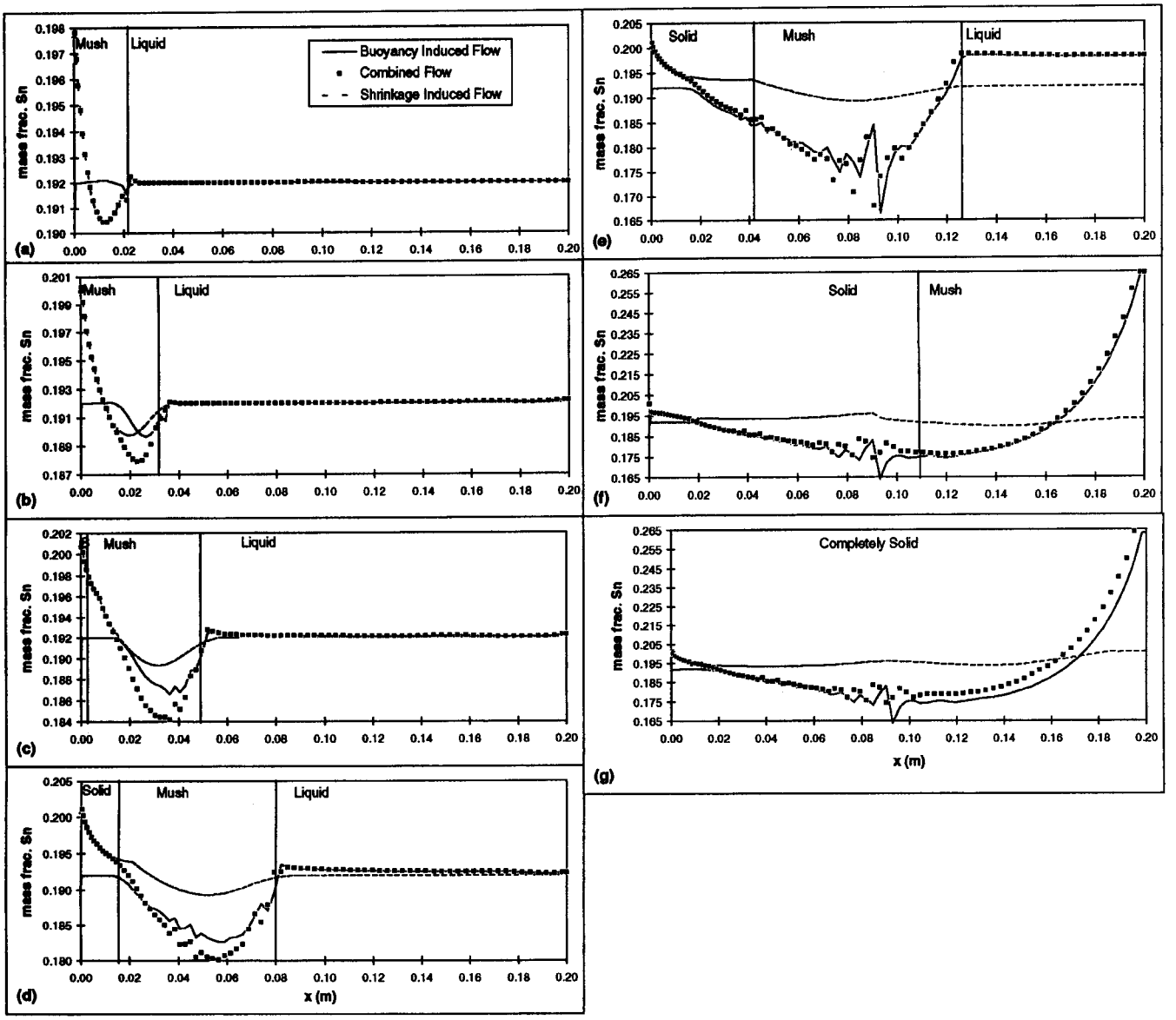

Fig. 6—Midheight composition profiles, U = 1000 W/m² K, at (*a*) 25 s, (*b*) 50 s, (*c*) 100 s, (*d*) 200 s, (*e*) 400 s, (*f*) 1000 s, and (*g*) 1750 s.

At t = 1000 seconds (Figure 6(f)), the solid region covers more than half the domain. In the mushy zone, which encompasses the rest of the mold, solute redistribution is completely controlled by buoyancy-driven flows, and there is little change in the Sn profile to the time of complete solidification at t = 1750 seconds (Figures 6(g) and 9). These plots show three prominent regions of macrosegregation. The tin-rich zone near the chilled wall results from the relatively strong shrinkage-induced flow early in the process. In the middle of the domain, a large, broad tin-depleted cone rises from the bottom of the ingot. In this region, negative segregation is compounded by the presence of several freckles. Most of the tin rejected during primary solidification is found in a third region near the riser, which is the last to solidify and therefore is characterized by a large Sn concentration.

Re-examining concentration distributions for the earlier stages of solidification, one is prompted to conclude that shrinkage strongly influences the model predictions. Certainly, at those times, shrinkage-driven flows play a major role in transporting solute through the mushy zone. However, while positive segregation near the cold wall caused by contraction of the alloy (+0.9 pct) is about half that associated with the negative cone segregate in the primary center of the ingot (−1.5 pct), the banded segregation at the right wall is dominant (+7.0 pct). Given that the region in which shrinkage dominates the distribution of solute is relatively small (less than 10 pct of the total ingot) and that the level of macrosegregation in this region is approximately 10 pct of that in the far end of the domain, one can conclude that, in this case, shrinkage has a second-order effect on macrosegregation.

With U = 10,000 W/m² K, the rate of heat extraction is large and the chilled wall temperature decreases from its initial value of 560 to 315 K (≈95 pct of the difference between the initial and coolant temperatures) in approximately 60 seconds. Such a large heat-transfer coefficient approximates the use of nucleate boiling to cool the ingot and yields a thermal boundary condition comparable to that associated with maintaining an isothermal mold wall. This condition is extremely favorable to enhancing the effect of shrinkage-induced flow on solutal redistribution.

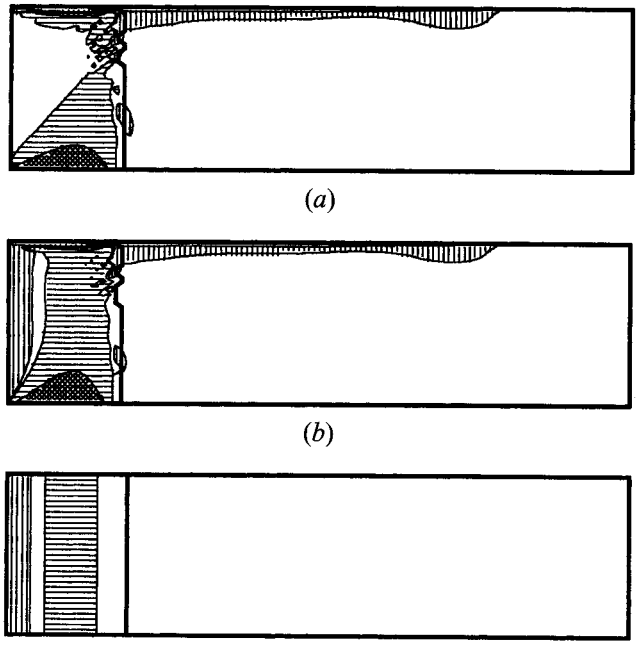

Fig. 7—Macrosegregation plots at 50 s for U = 1000 W/m² K: (*a*) buoyancy-induced flow, (*b*) buoyancy- and shrinkage-induced flow, and (*c*) shrinkage-induced flow (same legend as in Fig. 3).

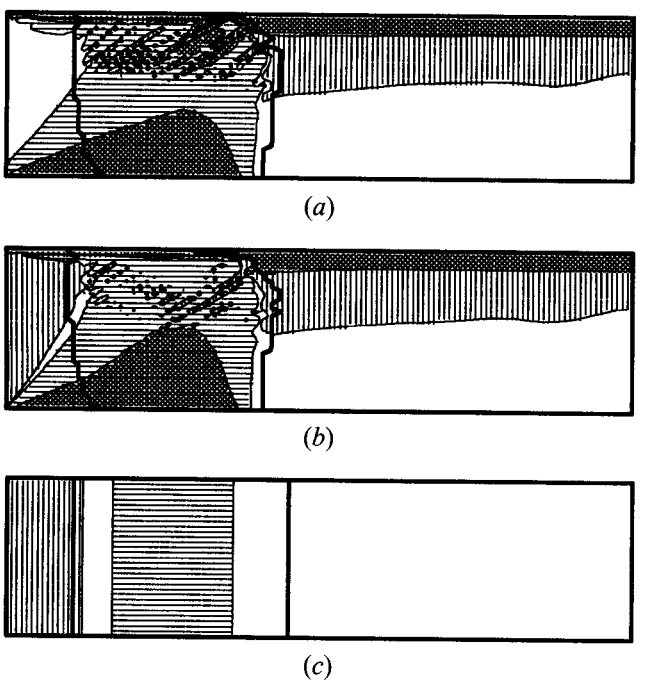

Fig. 8—Macrosegregation plots at 200 s for U = 1000 W/m² K: (*a*) buoyancy-induced flow, (*b*) buoyancy- and shrinkage-induced flow, and (*c*) shrinkage-induced flow (same legend as in Fig. 3).

Figure 10(a) shows the midheight composition profiles at t = 10 seconds. In a 5-mm-thick region adjoining the chilled wall, there is significant positive segregation (+1.8 pct) due to the large rate of latent heat release occurring within the first few seconds. The correspondingly large shrinkage-induced velocity advects most of the rejected tin toward the chilled surface, and there is excellent agreement between the solute profiles in the mush for predictions based on the combined and shrinkage flow conditions. As

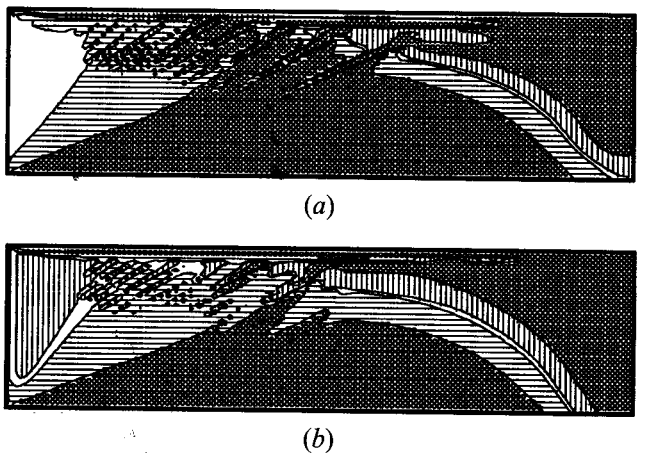

Fig. 9—Macrosegregation plots at 1750 s for U = 1000 W/m² K: (*a*) buoyancy-induced flow and (*b*) buoyancy- and shrinkage-induced flow (same legend as in Fig. 3).

shown in Figure 11, the macrosegregation pattern for the combined flow is controlled almost entirely by shrinkage effects. If the flow is assumed to be driven solely by buoyancy, the progression of the solidification fronts is rapid enough to fix the initial composition everywhere but very close to the top and bottom of the ingot.

At t = 50 seconds, Figure 12 reveals that, while becoming more significant, buoyancy effects influence macrosegregation only near the top and bottom of the domain. Figure 10(b) suggests that buoyancy is becoming influential near the liquidus interface, but nowhere is it the dominant effect. Figures 10(c) through (e) demonstrate the same type of progression from shrinkage- to buoyancy-controlled conditions in the mush which occurred for U = 1000 W/m² K. The time period over which this transition occurs is only slightly shorter for U = 10,000 W/m² K than for U = 1000 W/m² K.

Complete solidification occurs at approximately 1400 seconds (Figure 13), and the region in which macrosegregation is controlled by shrinkage effects encompasses approximately 15 to 20 pct of the total domain. Although the extent of this region exceeds that associated with U = 1000 W/m² K, concentrations in this part of the ingot are within ≈0.2 pct of the composition in the buoyancy case. Due to the high solidification rate, especially early in the process, there is less buoyancy-driven macrosegregation than for the previous cases. However, the negatively segregated cone in the middle of the domain (−1.5 pct along the midheight) and the tin-rich band at the far end (+7.0 pct) are still much larger than the shrinkage-induced redistribution at the chilled wall. Even at this high level of heat extraction, and therefore large U_s, the shrinkage-driven transport of solute is only significant near the chilled wall and makes a small contribution to overall macrosegregation in the final ingot.

V. SIMILARITY CONSIDERATIONS

The foregoing numerical simulations have shown that shrinkage-induced flows have a small effect on the final macrosegregation patterns for a particular Pb-Sn system. Thermal boundary conditions ranged from a comparatively small heat extraction rate, for which shrinkage had no discernable effect, to a large rate, for which shrinkage effects

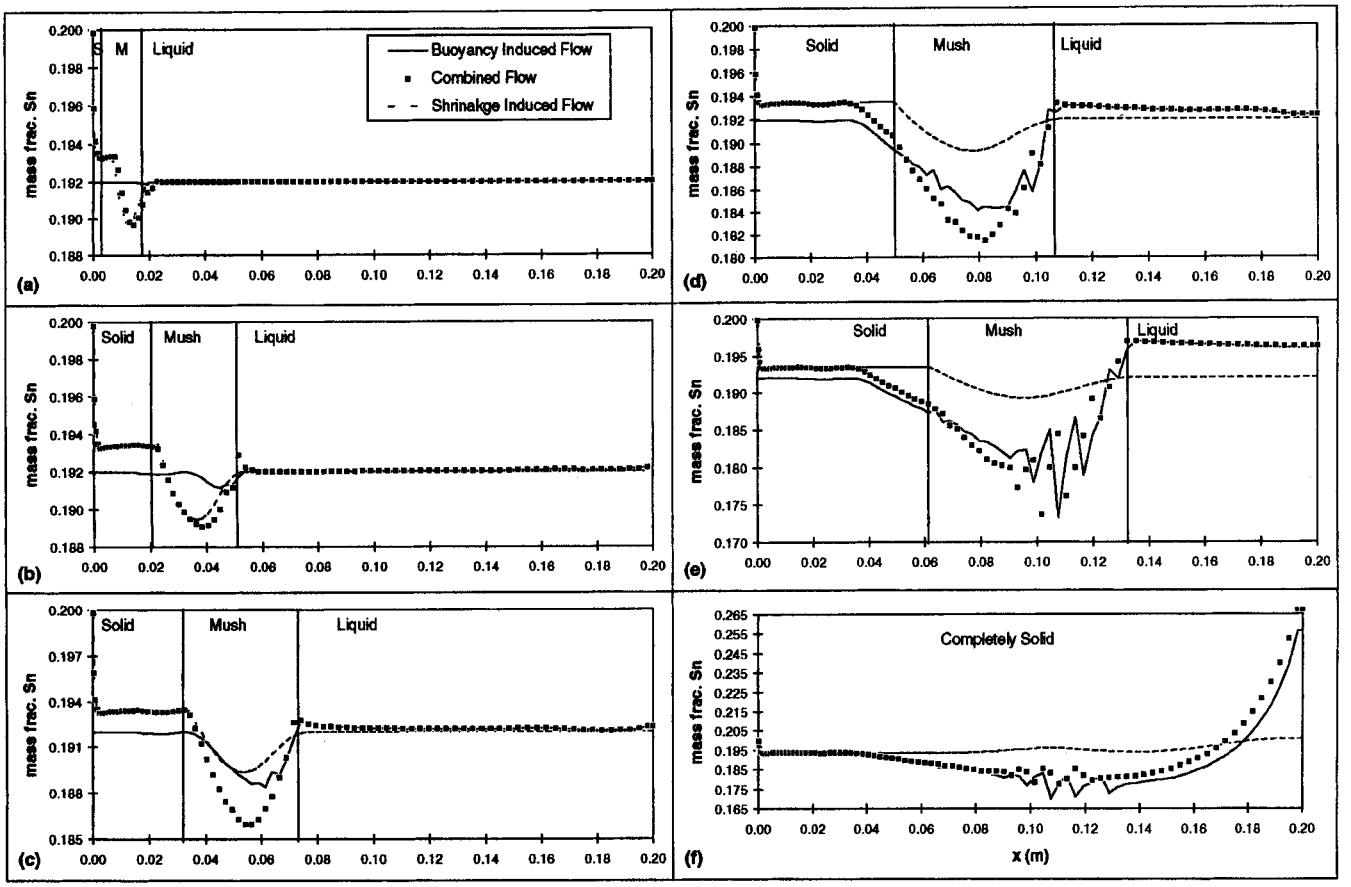

Fig. 10—Midheight composition profiles, U = 10,000 W/m² K, at (*a*) 10 s, (*b*) 50 s, (*c*) 100 s, (*d*) 200 s, (*e*) 300 s, and (*f*) 1400 s.

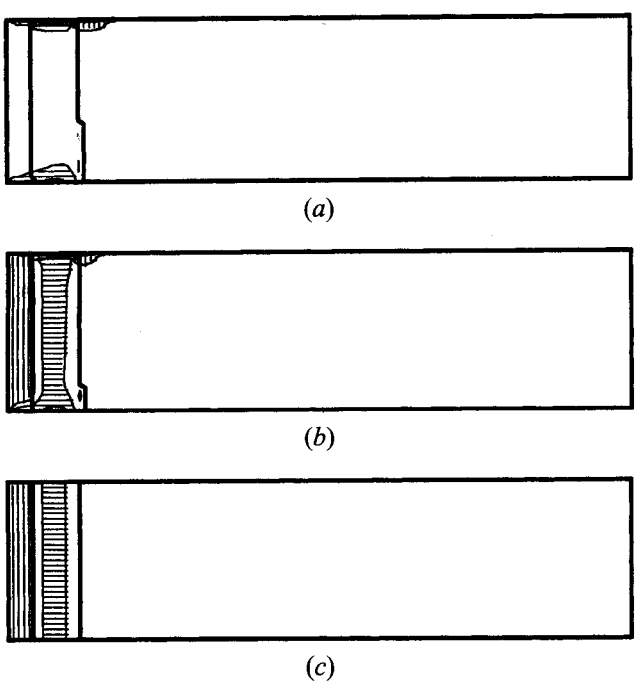

Fig. 11—Macrosegregation plots at 10 s for U = 10,000 W/m² K: (*a*) buoyancy-induced flow, (*b*) buoyancy- and shrinkage-induced flow, and (*c*) shrinkage-induced flow (same legend as in Fig. 3).

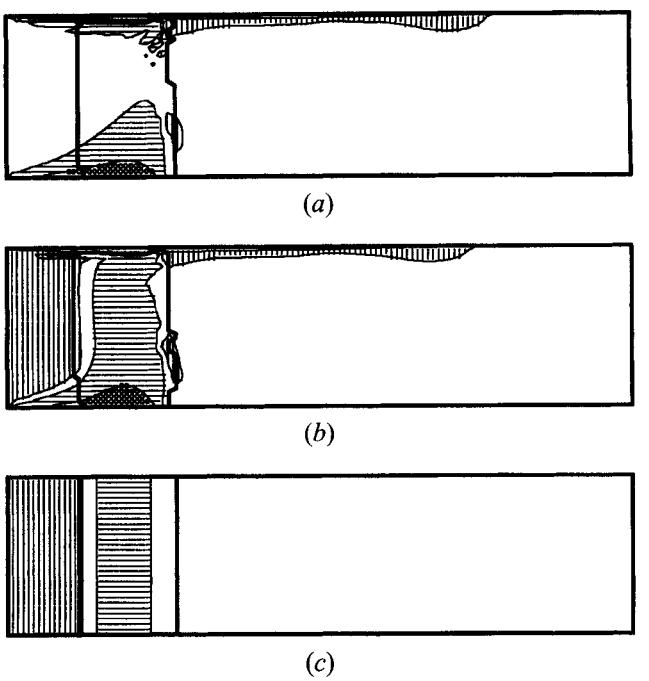

Fig. 12—Macrosegregation plots at 50 s for U = 10,000 W/m² K: (*a*) buoyancy-induced flow, (*b*) buoyancy- and shrinkage-induced flow, and (*c*) shrinkage-induced flow (same legend as in Fig. 3).

were restricted to early flow and solute redistribution patterns in the mushy zone. The question of applicability of these results to other binary systems is addressed by considering the reference velocities developed in the scaling analysis. The reference velocities provide a measure of the strength of the buoyancy- and shrinkage-induced flows in a side-cooled alloy and can be contrasted for different al-

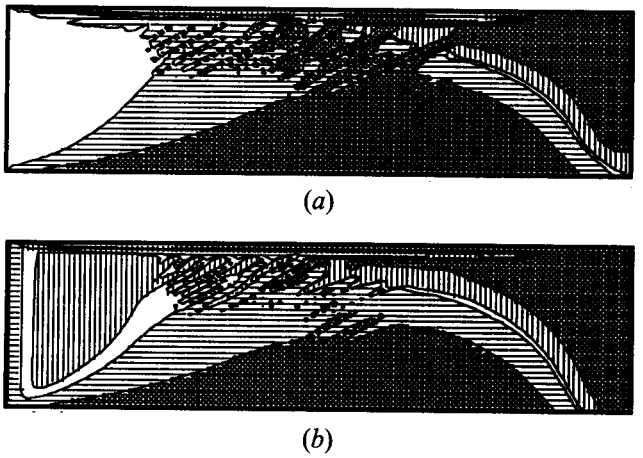

(*a*)

(*b*)

Fig. 13—Macrosegregation plots at 1400 s for U = 10,000 W/m² K: (*a*) buoyancy-induced flow and (*b*) buoyancy- and shrinkage-induced flow (same legend as in Fig. 3).

loys. As examples, Al-5.65 pct Cu and Cu-13.5 pct Sn will be compared to the Pb-19.2 pct Sn system.

From Eq. [16], the ratio of buoyancy velocities for Pb-Sn and Al-Cu may be expressed as

$$U_b|_{\text{Al-Cu}} / U_b|_{\text{Pb-Sn}} = \left[\frac{\rho_l \beta_S \Delta f_l^\alpha}{\mu_l}\right]_{\text{Al-Cu}} \left[\frac{\mu_l}{\rho_l \beta_S \Delta f_l^\alpha}\right]_{\text{Pb-Sn}} \quad [21]$$

which assumes an equivalent dependence of the permeability of the two systems on the solid volume fraction. Although the solutal and thermal buoyancy forces for the Al-Cu mixture are both downward, Mehrabian *et al.*[32] and Mori and Ogi[33] have shown that macrosegregation patterns in a side-cooled Al-Cu ingot are similar to the numerical results of this study (Figures 5, 9, and 13). The major difference is that due to the downward buoyancy force, the channels are oriented down and to the right (as opposed to the current Pb-Sn results, in which channels extend up and to the right). The scaling parameters of this study remain valid because the buoyancy force is still perpendicular to the direction of shrinkage-induced flow. Using properties from Table I, Diao and Tsai,[21] and Brandes and Brook,[20] Eq. [21] yields

$$|U_b|_{\text{Al-Cu}} / |U_b|_{\text{Pb-Sn}} \approx 1.91 \quad [22]$$

For the Cu-Sn system, $(\beta_s \Delta f_l^\alpha / \beta_T \Delta T)$ is close to unity. Therefore, the buoyancy velocity must account for both thermal and solutal effects and is written as

$$U_b \sim \frac{\rho_l g(\beta_S \Delta f_l^\alpha + \beta_T \Delta T)K}{\mu_l} \quad [23]$$

Using Eq. [23] for the Cu-Sn system and Eq. [16] for Pb-Sn, the ratio of buoyancy velocities is

$$U_b|_{\text{Cu-Sn}} / U_b|_{\text{Pb-Sn}} \approx 0.0066 \quad [24]$$

From Eq. [20], the ratio of shrinkage velocities may be expressed as

$$U_s|_{\text{Al-Cu}} / U_s|_{\text{Pb-Sn}} = \left[\left(\frac{q_{\text{lat}}}{H}\right)\frac{\beta}{\rho_s h_f}\right]_{\text{Al-Cu}} \left[\left(\frac{H}{q_{\text{lat}}}\right)\frac{\rho_s h_f}{\beta}\right]_{\text{Pb-Sn}} \quad [25]$$

The latent heat release rate per unit surface area may be reasonably approximated as $(q_{\text{lat}}/H) \sim U(T_s - T_c)$. Assuming equivalent heat-transfer coefficients for both systems, it follows that

$$U_s|_{\text{Al-Cu}} / U_s|_{\text{Pb-Sn}} = \left[\frac{(T_s - T_c)\beta}{\rho_s h_f}\right]_{\text{Al-Cu}} \left[\frac{\rho_s h_f}{(T_s - T_c)\beta}\right]_{\text{Pb-Sn}} \approx 0.83 \quad [26]$$

and

$$U_s|_{\text{Cu-Sn}} / U_s|_{\text{Pb-Sn}} \approx 1.11 \quad [27]$$

While Eqs. [22] and [26] indicate that the characteristic shrinkage and buoyancy velocities for the Al-Cu system are approximately 20 pct smaller and 100 pct larger, respectively, than those of the Pb-Sn system, the ratios are of order unity, suggesting similar macrosegregation trends for the two cases. Hence, relative to the influence of buoyancy, one would not expect the Al-Cu system to experience significant macrosegregation due to shrinkage effects. However, for Cu-Sn, the two-orders-of-magnitude reduction in the buoyancy velocity and the slight increase in the shrinkage velocity suggest that shrinkage effects would strongly influence macrosegregation in this system.

VI. CONCLUSIONS

The effect of solidification shrinkage on macrosegregation in a binary alloy chilled from one side has been examined using a continuum model. A scaling analysis of the momentum equations produces reference velocities for shrinkage- and buoyancy-induced flows, which may be used to assess their relative strength for different alloys. For a Pb-19.2 pct Sn system, predicted macrosegregation patterns were compared at three different cooling rates for shrinkage-induced flow, buoyancy-induced flow, and a combined flow condition. While shrinkage may have other effects unexamined here (*e.g.*, porosity and hot tears), the comparisons show that macrosegregation patterns are dominated by buoyancy effects, except for large cooling rates. Shrinkage effects become more important with increasing cooling rate, but even for the largest rate considered in this study, the influence on macrosegregation is restricted to a small region near the chilled, vertical surface. This result is quite different than the dominant effect of shrinkage-induced flow on solute redistribution during stable solidification from below. Comparisons of the reference velocities suggest that similar behavior characterizes an Al-5.65 pct Cu system, but that shrinkage effects are more important for a Cu-13.5 pct Sn alloy.

TABLE OF SYMBOLS

A_m	frontal area of mushy zone (m²)
c	specific heat (J/kg K)
D_l	mass diffusion coefficient (m²/s)
f	mass fraction
f^α	mass fraction of species α
g	volume fraction or gravitational acceleration (m/s²)
h	enthalpy (J)
h_f	heat of fusion (J/kg)
H	height of domain (m)

k	thermal conductivity (W/m K)
K	permeability (m^2)
L_1	length of bottom wall (m)
L_2	length of top wall (m)
m	mass (kg)
P	pressure (N/m^2)
q_{lat}	latent heat extraction rate (W)
t	time (s)
T	temperature (K)
u	x velocity (m/s)
U	reference velocity (m/s), overall heat-transfer coefficient (W/m^2 K)
v	y velocity (m/s)
$\mathbf{V}$	velocity vector (m/s)
V	volume (m^3)
x,y	Cartesian coordinates (m)

Greek Symbols

α	thermal diffusivity (m^2/s)
β	contraction ratio
β_s	solutal expansion coefficient
β_T	thermal expansion coefficient (1/K)
δ	mushy zone thickness (m)
κ_0	permeability constant (m^2)
μ_l	dynamic viscosity (kg/s m)
ρ	density (kg/m^3)

Subscripts

b	buoyancy driven
c	chill
d	diffusion driven
e	eutectic
l	liquid
0	initial
s	solid, shrinkage driven
S	solutal
T	thermal

Superscripts

α	constituent of binary mixture

ACKNOWLEDGMENTS

The authors would like to thank the Department of Energy for support through Award Number DE-FG02-87ER13759. One of the authors (MJMK) would also like to thank Dr. Jun Ni and Professor Satish Ramadhyani for many useful discussions during the course of this work.

REFERENCES

1. W.D. Bennon and F.P. Incropera: *Int. J. Heat Mass Transfer*, 1987, vol. 30, pp. 2161-70.
2. V.R. Voller and C. Prakash: *Int. J. Heat Mass Transfer*, 1987, vol. 30, pp. 1709-19.
3. C. Beckermann and R. Viskanta: *PCH Physicochem. Hydrodyn.*, 1988, vol. 10, pp. 195-213.
4. S. Ganesan and D.R. Poirier: *Metall. Trans. B*, 1990, vol. 21B, pp. 173-81.
5. G. Amberg: *Int. J. Heat Mass Transfer*, 1991, vol. 34, pp. 217-27.
6. J. Ni and C. Beckermann: *Metall. Trans. B*, 1991, vol. 22B, pp. 349-61.
7. P.J. Prescott, F.P. Incropera, and W.D. Bennon: *Int. J. Heat Mass Transfer*, 1991, vol. 34, pp. 2351-59.
8. S.D. Felicelli, J.C. Heinrich, and D.R. Poirier: *Metall. Trans. B*, 1991, vol. 22B, pp. 847-59.
9. D.G. Neilson and F.P. Incropera: *Int. J. Heat Mass Transfer*, 1991, vol. 34, pp. 1717-32.
10. M.C. Flemings and G.E. Nereo: *Trans. TMS-AIME*, 1967, vol. 239, pp. 1449-61.
11. M.C. Flemings, R. Mehrabian, and G.E. Nereo: *Trans. TMS-AIME*, 1968, vol. 242, pp. 41-49.
12. M.C. Flemings and G.E. Nereo: *Trans. TMS-AIME*, 1968, vol. 242, pp. 50-55.
13. R. Mehrabian, M. Keane, and M.C. Flemings: *Metall. Trans.*, 1970, vol. 1, pp. 1209-20.
14. N. Streat and F. Weinberg: *Metall. Trans.*, 1974, vol. 5, pp. 2539-48.
15. F.C. Chang and H.L. Tsai: in *Transport Phenomena in Material Processing*, ASME HTD 132, M. Charmichi, M.K. Chyu, Y. Joshi, and S.M. Walsh, eds., ASME, Fairfield, NJ, 1992, pp. 73-80.
16. R. Viskanta: in *Solar Heat Storage: Latent Heat Materials*, G.A. Lane, ed., CRC Press, Boca Raton, FL, 1983, vol. I, pp. 153-222.
17. D. Xu and Q. Li: *Numer. Heat Transfer A*, 1991, vol. 20, pp. 203-11.
18. K.C. Chiang and H.L. Tsai: *Int. J. Heat Mass Transfer*, 1992, vol. 35, pp. 1763-70.
19. K.C. Chiang and H.L. Tsai: *Int. J. Heat Mass Transfer*, 1992, vol. 35, pp. 1771-78.
20. *Smithell's Metals Reference Handbook*, 7th ed., E.A. Brandes and G.B. Brook, eds., Butterworth-Heinemann, Ltd., Oxford, United Kingdom, 1992.
21. Q.Z. Diao and H.L. Tsai: *Metall. Trans. A*, 1993, vol. 24A, pp. 963-73.
22. G. Amberg: in *Interactive Dynamics of Convection and Solidification*, S.H. Davis, H.E. Huppert, U. Muller, and M.G. Worster, eds., Kluwer, Amsterdam, 1992.
23. G. Amberg: Report No. TRITA-MEK TR 1993:9, The Royal Institute of Technology, Stockholm, 1993.
24. W.D. Bennon and F.P. Incropera: *Numer. Heat Transfer*, 1988, vol. 13, pp. 277-96.
25. R. Nasser-Rafi, R. Deshmukh, and D.R. Poirier: *Metall. Trans. A*, 1985, vol. 16A, pp. 2263-71.
26. S. Patankar: *Numerical Heat Transfer and Fluid Flow*, Hemisphere, New York, NY, 1980, pp. 131-34.
27. L. Wang, V. Laxmanan, and J.F. Wallace: *Metall. Trans. A*, 1988, vol. 19A, pp. 2687-94.
28. M.C. Schneider and C. Beckermann: *Transport Phenomena in Solidification*, ASME HTD 284, ASME, Fairfield, NJ, 1994, pp. 43-58.
29. P.J. Prescott and F.P. Incropera: *ASME JHT*, 1994, vol. 116, pp. 735-41.
30. A. Bejan: *Convective Heat Transfer*, Wiley-Interscience, New York, NY, 1984, pp. 389-91.
31. P.J. Prescott, F.P. Incropera, and D.R. Gaskell: *ASME JHT*, 1994, vol. 116, pp. 742-49.
32. R. Mehrabian, M. Keane, and M.C. Flemings: *Metall. Trans.*, 1970, vol. 1, pp. 3238-41.
33. N. Mori and K. Ogi: *Metall. Trans. A*, 1991, vol. 22A, pp. 1663-72.